Supporting Information

Pressure-induced dehydration and reversible recrystallization of dihydrogen-bonded sodium borohydride dihydrate $NaBH_4 \cdot 2H_2O$

Satoshi Nakano,[1,] Hiroshi Fujihisa,[2] Hiroshi Yamawaki,[2] Yuki Shibazaki,[3] Takumi Kikegawa,[3] Shin-ichi Orimo[4,5]*

[1]National Institute for Materials Science (NIMS), Tsukuba, Ibaraki 305-0044, Japan

[2]National Metrology Institute of Japan (NMIJ), National Institute of Advanced Industrial Science and Technology (AIST), Tsukuba, Ibaraki 305-8565, Japan

[3]Photon Factory (PF), Institute of Materials Structure Science (IMSS), High Energy Accelerator Research Organization (KEK), Tsukuba, Ibaraki 305-0801, Japan

[4]Advanced Institute for Materials Research (WPI-AIMR), Tohoku University, Sendai, Miyagi 980-8577, Japan

[5]Institute for Materials Research (IMR), Tohoku University, Sendai, Miyagi 980-8577, Japan

*Corresponding author: S. Nakano (Email: nakano.satoshi@nims.go.jp)

1. The estimation of crystallite sizes and strains of α-$NaBH_4$ and ice VII

In the Williamson-Hall method,[39] the X-ray peak broadening can be assumed to be a simple sum of the size broadening and the strain one, as in the following equation:

$$\beta = \beta_{strain} + \beta_{size} = C\varepsilon \tan\theta + K\lambda/(d \cos\theta) \quad \text{(Equation S1)}$$

where β, Cε, θ, K, λ, and d are the full width at half maximum (FWHM) of the peak (rad), the strain, the Bragg angle (rad), the Scherrer constant (assuming K = 0.9 here), the X-ray wavelength (nm), and the crystallite size (nm), respectively.

The average crystallite size d and the strain Cε are calculated from the intercept and the slope of the line, respectively, in the Williamson-Hall plot.

Figure S1 shows the Williamson-Hall plot of α-$NaBH_4$ and ice VII, which were decomposed from $NaBH_4 \cdot 2H_2O$, at 5.1 GPa, and that of the commercial α-$NaBH_4$ powder at AP for comparison. The d and Cε of α-$NaBH_4$ were estimated to 39 nm and 0.011, respectively, and those of ice VII were estimated to 24 nm and 0.009. The d and Cε of the commercial α-$NaBH_4$ powder were 52 nm and 0.0007, respectively. These data were listed in Table S1.

The data of the 111 peak of α-$NaBH_4$ decomposed from $NaBH_4 \cdot 2H_2O$ was excluded from the linear fitting as it was extremely far away from the data of other peaks. As this method assumes the uniform growth of crystallite size, the data for orientations with larger growth than other orientations deviate from the linear line. Crystallites of α-$NaBH_4$ decomposed from $NaBH_4 \cdot 2H_2O$ may have a relatively predominant growth in the 111 plane.

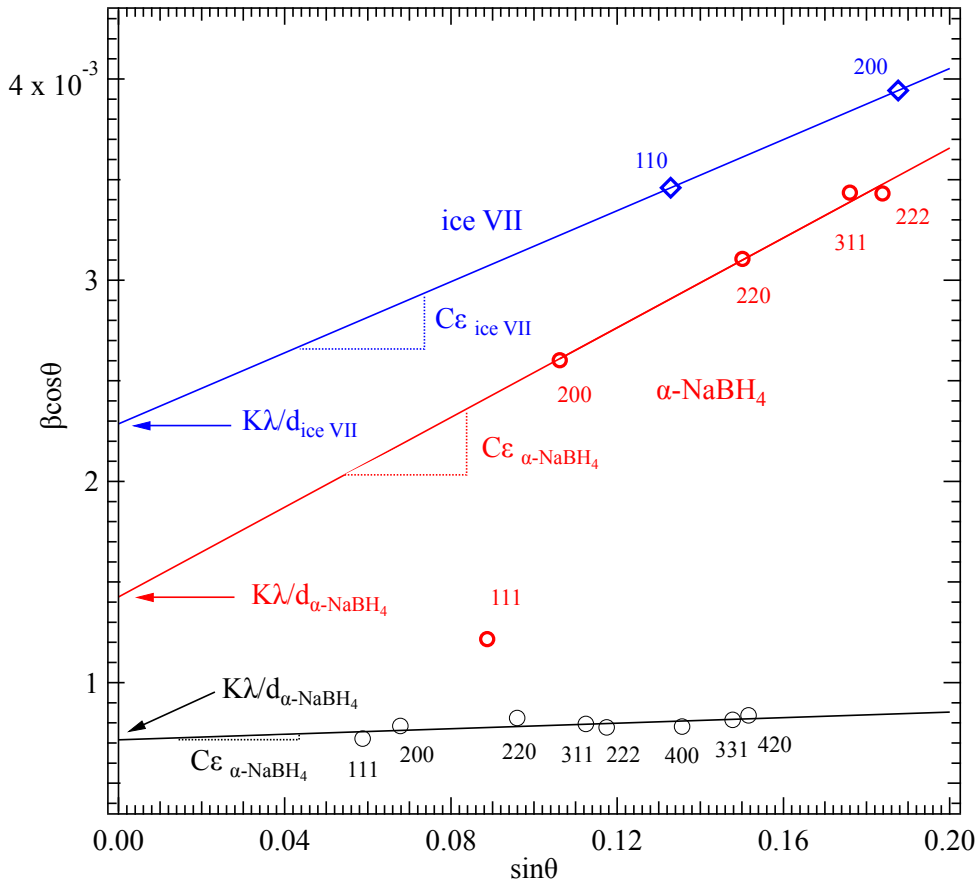

Figure S1. Crystallite size and strain calculation of α-$NaBH_4$ and ice VII decomposed from $NaBH_4 \cdot 2H_2O$ at 5.1 GPa using Williamson-Hall method. Red circles and blue squares represent the data of peaks of α-$NaBH_4$ and ice VII, respectively. Back circles represent that of a commercial α-$NaBH_4$ powder at ambient-pressure (AP) for comparison. The three digit number represents the Miller index.

Table S1. Crystallite sizes (d) and strains (Cε) determined using the Williamson-Hall plot.

Sample	Pressure (GPa)	d (nm)	Cε
Product decomposed from $NaBH_4 \cdot 2H_2O$			
α-$NaBH_4$	5.1	39	0.011
ice VII	5.1	24	0.009
Chemical purchased			
α-$NaBH_4$	0	52	0.0007

2. Pressure-induced transformation of $NaBH_4$ with a helium medium

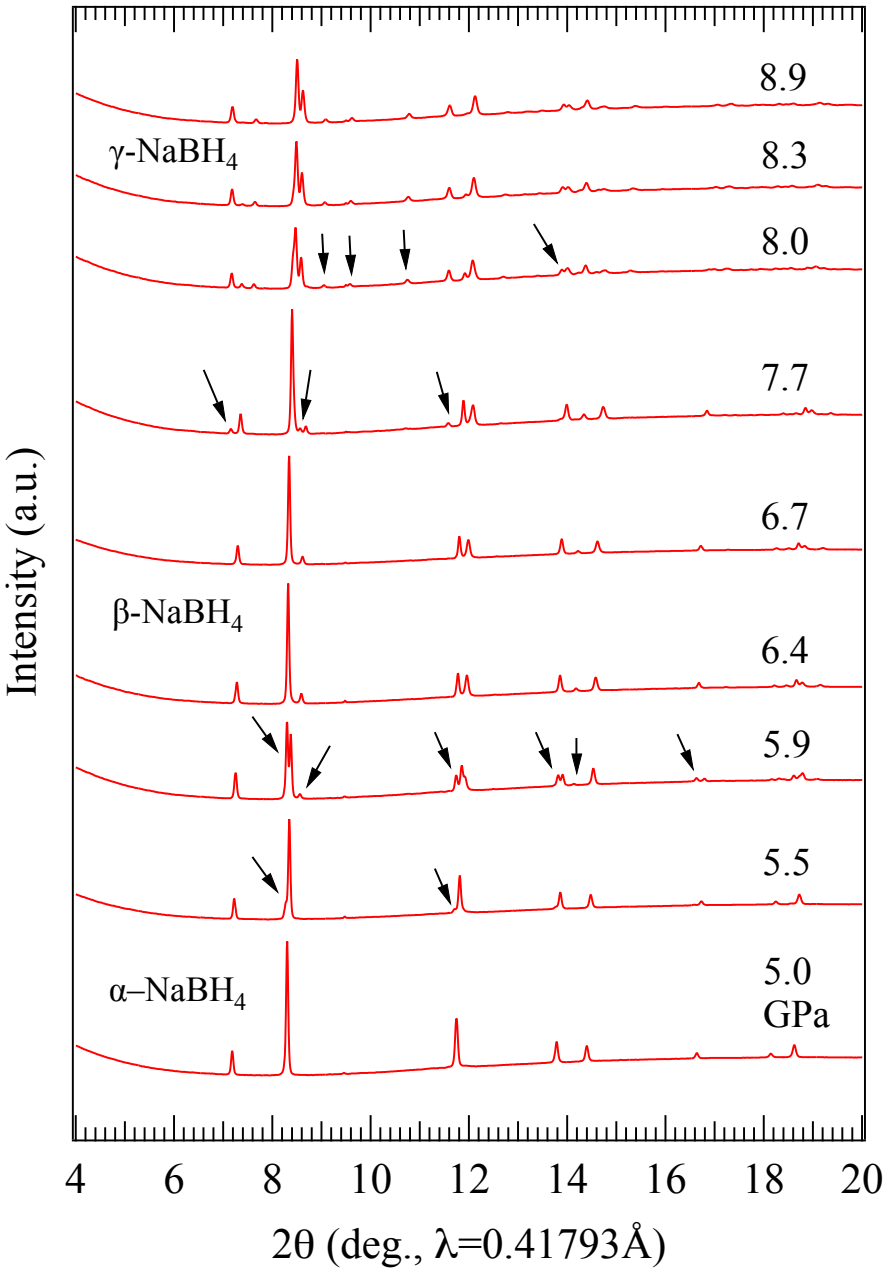

Figure S2. Pressure dependence of the X-ray diffraction (XRD) pattern of $NaBH_4$ with a helium pressure medium during compression. Black arrows indicate the appearance of new peaks. The transformation from α-$NaBH_4$ to β-$NaBH_4$ started at 5.5 GPa and completed at 6.4 GPa, and then the next transformation to γ-$NaBH_4$ started at 7.0 GPa.

3. Comparison of the dehydration of $NaBH_4 \cdot 2H_2O$ with those of hydrous compounds due to hydrogen bonding

It is valuable to compare the pressure-induced dehydration reactions of dihydrogen-bonded $NaBH_4 \cdot 2H_2O$ with those of hydrogen-bonded hydrous compounds.

Many hydrous minerals and inorganic compounds contain water of crystallization bonded by hydrogen bonds. In geochemistry, the dehydration reactions of these hydrous minerals under HP/HT conditions have been extensively studied, particularly in relation to water reservoirs in the Earth's interior and tectonic processes.[51] Several hydrous compounds, such as $Na_2SO_3 \cdot 7H_2O$,[52] $MgSO_4 \cdot 7H_2O$ (epsomite),[53] $CoSO_4 \cdot 7H_2O$ and $CoSO_4 \cdot 6H_2O$,[54] and $Cu_6Si_6O_{18} \cdot 6H_2O$ (dioptase),[55] exhibit pressure-induced dehydration even at RT. These compounds release their water of crystallization under pressure and form anhydrous compounds or hydrous compounds with a lower degree of hydration. In addition, amorphous calcium carbonate ($CaCO_3 \cdot nH_2O$) undergoes crystallization into calcite and vaterite upon compression.[56]

Among these compounds, neutron diffraction measurements of $MgSO_4 \cdot 7H_2O$ revealed the presence of ice VII following dehydration. However, in other experiments, H_2O crystals were not observed. This may be attributed to the slow diffusion rate of H_2O after dehydration due to the surrounding environment, or the possibility of an amorphous metastable state preventing the growth of H_2O crystals to a size detectable by XRD measurements. In this study, the crystallite size of ice VII was estimated to be over 24 nm, suggesting that the water molecules released from $NaBH_4 \cdot 2H_2O$ diffused several tens of nanometers before crystallizing.

Furthermore, $MgSO_4 \cdot 7H_2O$ and $CoSO_4 \cdot 6H_2O$ both demonstrated reversible reformation of their original compounds during decompression. In the case of $CoSO_4 \cdot 6H_2O$, relatively strong peaks were observed, indicating significant grain growth during recrystallization, a phenomenon similar to the recrystallization of $NaBH_4 \cdot 2H_2O$ observed in this study.

In conclusion, the pressure-induced dehydration and reversible recrystallization observed in this study are not phenomena unique to dihydrogen-bonded compounds. Similar behavior has been documented in some hydrogen-bonded hydrous compounds. However, it is important to note that such phenomena have only been confirmed in a limited number of hydrous sulfates, despite the large variety of hydrous compounds with hydrogen bonds. This may be due to the difference in the environment surrounding the water molecule, whether it is ions composed of oxygen, such as sulfate ions, carbonate ions, and silicate ions, or ions composed of hydrogen, such as BH_4^-. In any case, this further highlights that dihydrogen bonds are as strong as conventional hydrogen bonds.

REFERENCES

(51) Schmidt M. W.; Poli, S. Experimentally based water budgets for dehydrating slabs and consequences for arc magma generation *Earth Planet. Sci. Lett.* **1998,** *163* (1–4), 361–379, DOI: 10.1016/S0012-821X(98)00142-3

(52) Sood, R. R.; Stager, R. A. Pressure-Induced Dehydration Reactions and Transitions in Inorganic Hydrates *Science*, **1966**, 154 (3747), 388–390, DOI: 10.1126/science.154.3747.388

(53) Gromnitskaya, E. L.; Yagafarov, O. F.; Lyapin, A. G.; Brazhkin, V. V.; Wood, I. G.; Tucker M. G.; Fortes, A. D. The high-pressure phase diagram of synthetic epsomite ($MgSO_4 \cdot 7H_2O$ and

$MgSO_4 \cdot 7D_2O$) from ultrasonic and neutron powder diffraction measurements *Phys. Chem. Minerals* **2013**, *40* (3), 271–285, DOI 10.1007/s00269-013-0567-7

(54) Zhao, Z.; Kagi, H.; Komatsu, K.; Yamashita, K.; Nakano, S. Pressure-induced phase transitions of cobalt sulfate hydrates and discovery of a new high-pressure phase, $CoSO_4 \cdot 5H_2O$ *J. Solid State Chem.* **2022**, *308*, 122904-1–9, DOI: 10.1016/j.jssc.2022.122904

(55) Qin, F.; Wu, X.; Qin, S.; Zhang, D.; Prakapenka, V. B.; Jacobsen, S. D. Pressure-induced dehydration of dioptase: A single-crystal X-ray diffraction and Raman spectroscopy study *Comptes Rendus Geoscience* **2019**, *351* (2–3), 121–128, DOI: 10.1016/j.crte.2018.07.007

(56) Yoshino, T.; Maruyama, K.; Kagi, H.; Nara, M.; Kim, J. C. Pressure-Induced Crystallization from Amorphous Calcium Carbonate *Cryst. Growth Des.*, **2012**, *12* (7), 3357−3361, DOI: 10.1021/cg2017159

4. Pressure dependence of the volume of $NaBH_4$ decomposed from $NaBH_4 \cdot 2H_2O$

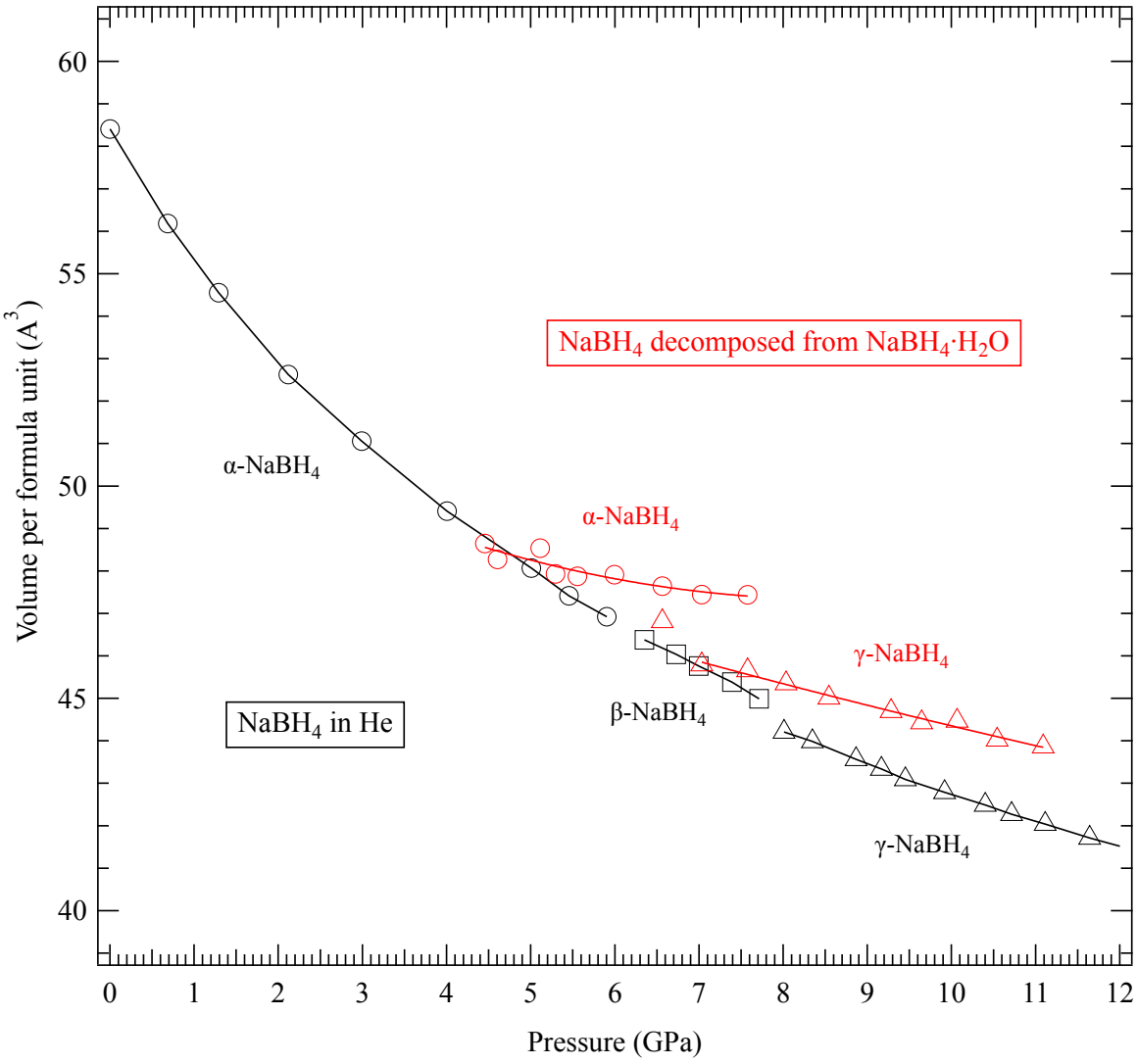

Figure S3. Pressure dependence of the volume of $NaBH_4$ decomposed from $NaBH_4 \cdot 2H_2O$ (red symbols) and that of $NaBH_4$ in helium pressure medium (black symbols).

5. Pressure dependence of the volume of ice VII decomposed from $NaBH_4 \cdot 2H_2O$

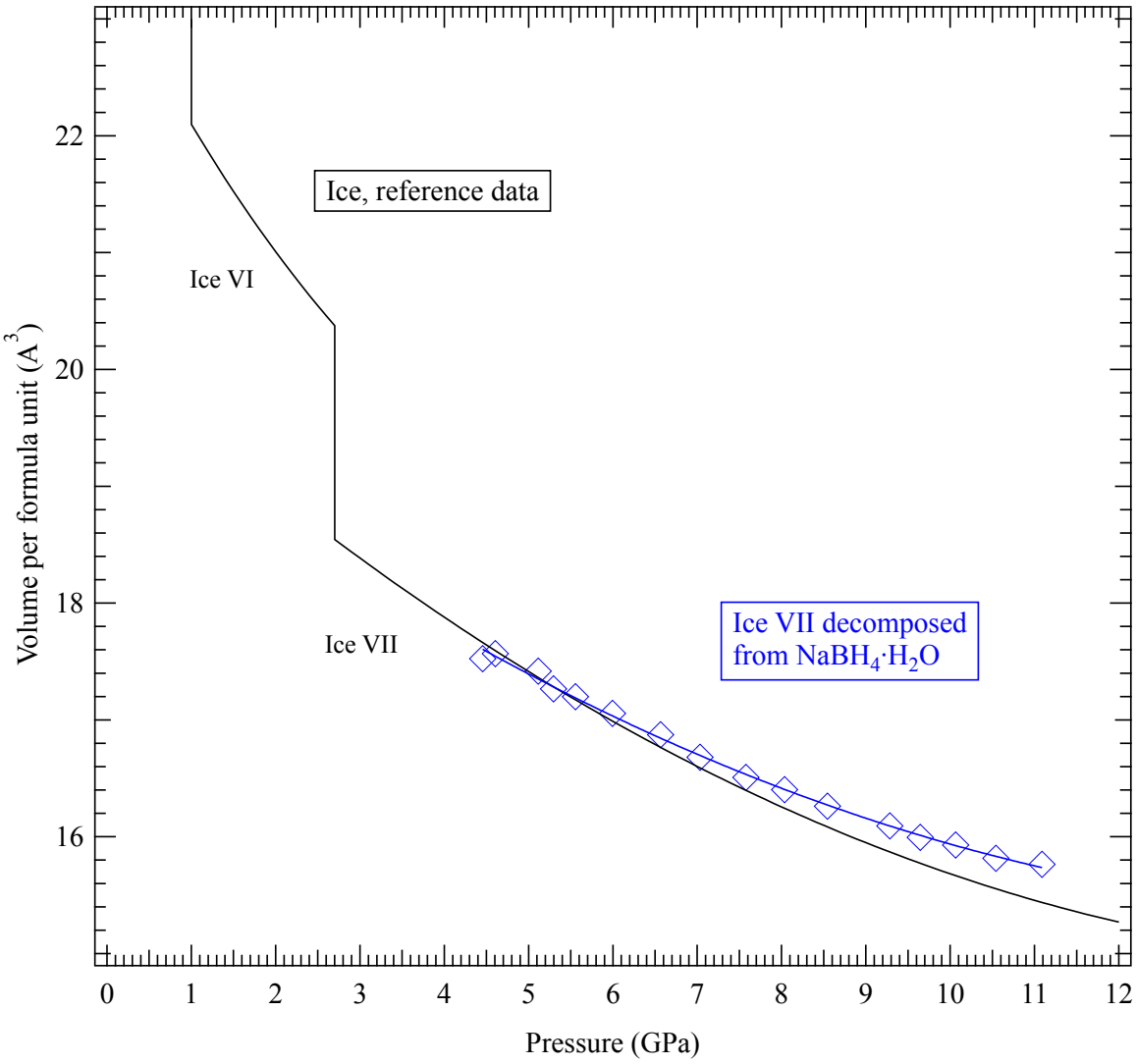

Figure S4. Pressure dependence of the volume of ice VII decomposed from $NaBH_4 \cdot 2H_2O$ (blue squares) and that of ice from the literature[46] (black line).

6. The influence of non-hydrostatic conditions in high-pressure XRD measurements using a diamond-anvil-cell (DAC)

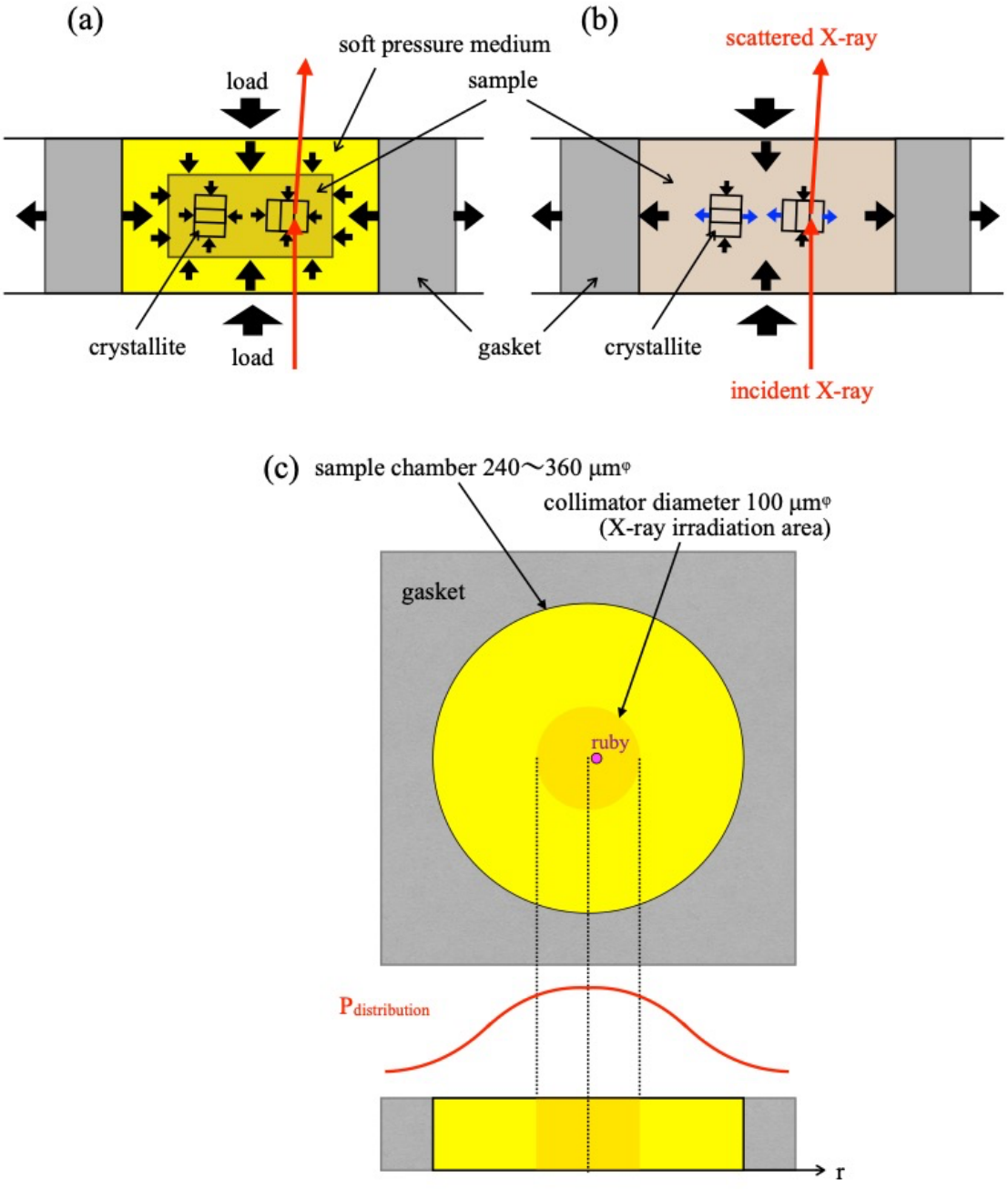

Figure S5. Schematic illustrations of the influence of non-hydrostatic conditions on the lattice parameters of observed in high-pressure XRD measurements using a diamond-anvil-cell (DAC): (a) hydrostatic condition with a soft pressure medium and (b) non-hydrostatic uniaxial-compressive condition without a pressure medium. (c) X-ray irradiation area viewed from the X-ray incidence direction and pressure distribution viewed perpendicular to the X-ray.

7. Crystallographic information of $NaBH_4 \cdot 2H_2O$

Table S2. Refinement parameters[a] of $NaBH_4 \cdot 2H_2O$ at 0.08 GPa and room temperature.

Space group: *Pbca*

a = 6.8789 Å, b = 12.1318 Å, c = 10.3587 Å

atom	x	y	z
Na	0.45557	0.01010	0.32564
B	0.09801	0.14978	0.38556
H1	0.08934	0.04896	0.38443
H2	0.00803	0.18989	0.29556
H3	0.02311	0.18145	0.48760
H4	0.26726	0.18043	0.38224
O1	0.14872	0.10525	0.01164
O2	0.24746	0.38825	0.18915
Hw1	0.10833	0.31931	0.49281
Hw2	0.28813	0.11283	0.02615
Hw3	0.26321	0.31649	0.22929
Hw4	0.19053	0.37108	0.10519

a) x, y, and z are the fractional position coordinates, and a, b, and c are the lattice parameters.

Table S3. Refinement parameters[a] of $NaBH_4 \cdot 2H_2O$ at 4.0 GPa and room temperature.

Space group: *Pbca*

a = 6.6020 Å, b = 11.6713 Å, c = 9.4943 Å

atom	x	y	z
Na	0.44120	0.00770	0.31896
B	0.10373	0.15333	0.38972
H1	0.08832	0.04947	0.39535
H2	0.02204	0.19261	0.28645
H3	0.01973	0.19183	0.49501
H4	0.28158	0.18092	0.39184
O1	0.15809	0.10059	0.02000
O2	0.27014	0.38041	0.19497
Hw1	0.11201	0.32140	0.50120
Hw2	0.30396	0.11004	0.03070
Hw3	0.27086	0.30715	0.24361
Hw4	0.21540	0.36147	0.10241

a) x, y, and z are the fractional position coordinates, and a, b, and c are the lattice parameters.

8. Symmetrized stress tensors calculated using DFT calculation with and without dispersion correction

Table S4. Comparison of symmetrized stress tensor of $NaBH_4 \cdot 2H_2O$ at 4.0 GPa calculated using DFT calculation with and without dispersion correction.

(a) With dispersion correction

Cartesian components (GPa)

	x	y	z
x	-2.086797	0.000000	0.000000
y	0.000000	-1.174897	0.000000
z	0.000000	0.000000	-2.027539

Pressure: 1.7631

(b) Without dispersion correction

Cartesian components (GPa)

	x	y	z
x	-3.915448	0.000000	0.000000
y	0.000000	-3.733713	0.000000
z	0.000000	0.000000	-4.318896

Pressure: 3.9894

9. Energy bands of $NaBH_4 \cdot 2H_2O$ calculated using DFT calculation

(a)

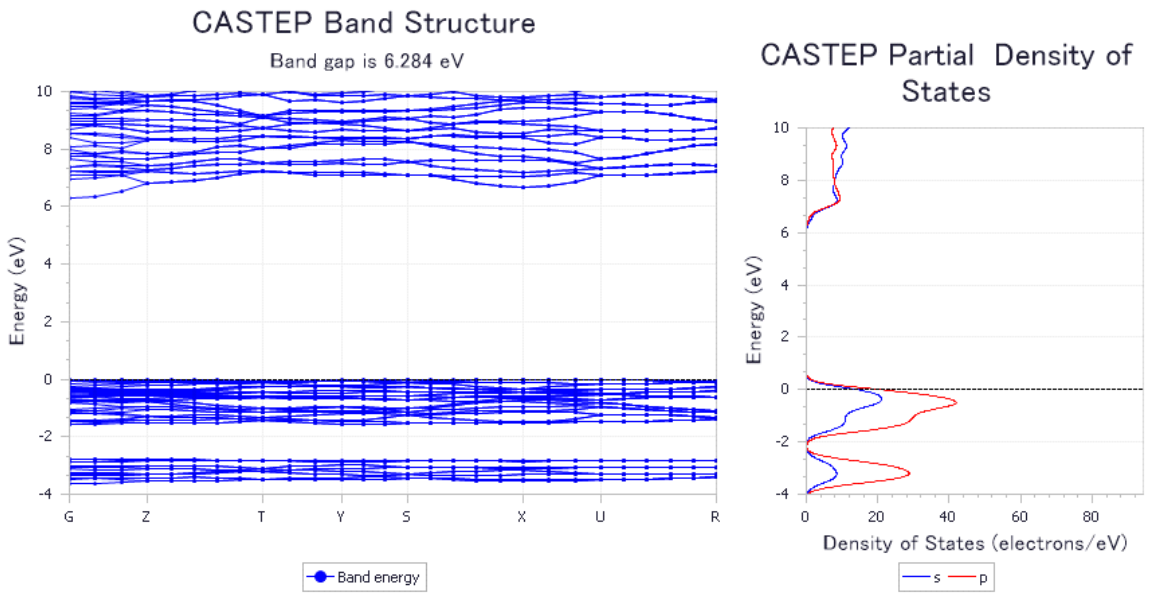

(b)

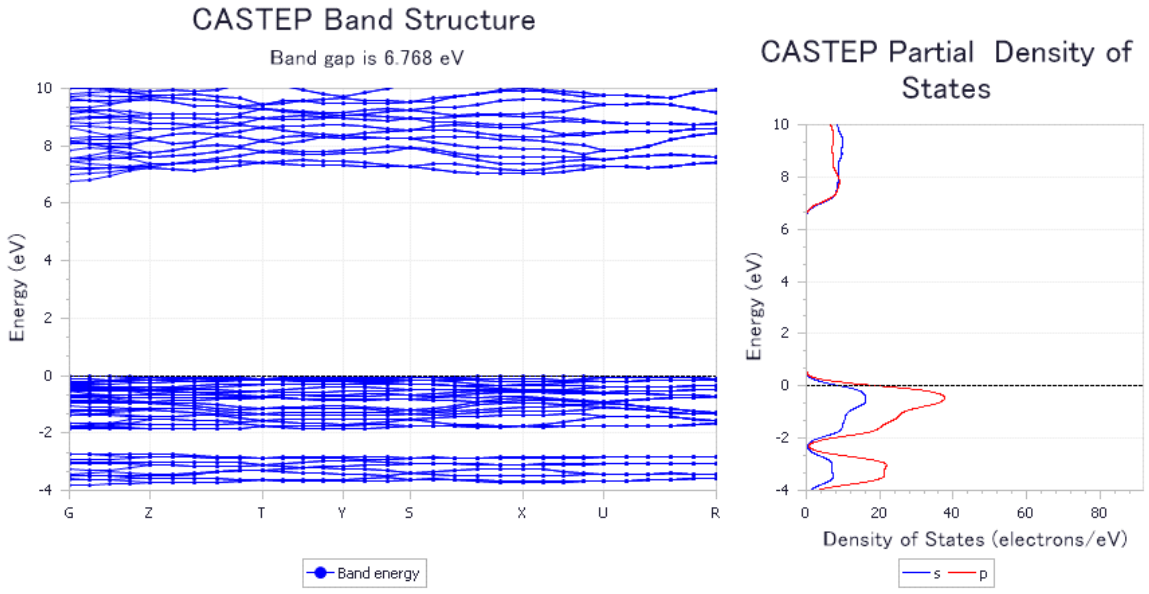

Figure S6. Energy bands of $NaBH_4 \cdot 2H_2O$ at (a) 0 GPa and (b) 4.0 GPa. Lattice constants and atomic coordinates were fully optimized before the band calculations. The $2s^2$ $2p^6$ electrons of Na, the $2s^2$ of B, and the $2s^2$ of O are located at deeper energy levels between −48 eV and −18 eV and are not shown here.